J Mater Sci (2008) 43:3596–3603
DOI 10.1007/s10853-008-2570-9

Preparation and thermophysical properties of $(Nd_xGd_{1-x})_2Zr_2O_7$ ceramics

Zhan-Guo Liu · Jia-Hu Ouyang · Yu Zhou

Received: 31 January 2008 / Accepted: 21 February 2008 / Published online: 23 March 2008

Abstract Ceramic powders of $(Nd_xGd_{1-x})_2Zr_2O_7$ ($x = 0$, 0.1, 0.3, 0.5, 0.7, 0.9, 1.0) were synthesized by chemical-coprecipitation followed by calcination method, and were then pressureless-sintered at 1,600 °C for 10 h in air. Phase constituents and morphologies of the synthesized powders and sintered ceramics were identified by X-ray diffraction (XRD), scanning electron microscopy (SEM), and transmission electron microscopy (TEM). A high-temperature dilatometer and a laser-flash method were used to analyze the thermal expansion coefficient and thermal diffusion coefficient of different ceramics from room temperature up to 1,400 °C. Thermal conductivity was calculated from thermal diffusivity, density, and specific heat. $(Nd_xGd_{1-x})_2Zr_2O_7$ ($0.1 \leq x \leq 1.0$) ceramics are with a pyrochlore-type structure; however, pure $Gd_2Zr_2O_7$ exhibits a defective fluorite-type structure. The average linear thermal expansion coefficients of different $(Nd_xGd_{1-x})_2Zr_2O_7$ ceramics decrease with increasing the value of x from 0 to 1.0 in the temperature range of 25–1,400 °C. The thermal conductivities of $(Nd_xGd_{1-x})_2Zr_2O_7$ ceramics are located within the range of 1.33 to 2.04 W m^{-1} K^{-1} from room temperature to 1,400 °C.

Introduction

Thermal barrier coatings (TBCs) are widely used in both diesel and gas turbine engines to protect hot-section metallic components from corrosion and oxidation at elevated temperatures, and to enhance component life and engine performance [1, 2]. Zirconia-based ceramic TBCs have attracted increasing attention for advanced engine applications due to their ability to provide thermal insulation for hot-section components. Some important requirements for good TBCs are low thermal conductivity, high thermal expansion coefficient, low Young's modulus, high-phase stability, and low sintering rate at elevated temperatures [3]. To further enhance operating efficiencies and reduce fuel consumption and gas emissions, it is urgently needed to develop new thermal barrier coating materials with increased phase stability, low lattice, and radiation thermal conductivity; and improved sintering resistance at extreme temperatures for future improvements in engine's performance to increase gas inlet temperatures to 1,650 °C or higher. However, the most commonly used TBC material of 6–8 wt.%Y_2O_3–ZrO_2 ceramics is limited if it is intended to operate over 1,200 °C. Above 1,200 °C, the t′-phase zirconia in TBCs transforms into cubic and tetragonal phases. During cooling the tetragonal phase will further transform into the monoclinic phase, which is accompanied with a volume change of 3–5% and a severe damage of TBCs. Two important groups of candidate materials with low thermal conductivity have emerged, one based on co-doping of YSZ with one or more rare-earth oxides and the other on the pyrochlore-type zirconates ($Ln_2Zr_2O_7$) [4, 5].

In recent years, there has been an increasing demand in developing TBCs with low thermal conductivity and high thermal stability. Among high-melting ceramic materials, rare-earth zirconates, with the general formula $Ln_2Zr_2O_7$ (Ln = rare-earth elements), have a distinct lower thermal conductivity than ZrO_2–Y_2O_3 ceramics. The thermal conductivities of $Ln_2Zr_2O_7$ (Ln = La, Nd, Sm, Eu, Gd, etc.) ceramics range from 1.1–2.0 W m^{-1} K^{-1} [5–8]. Mandal

Z.-G. Liu · J.-H. Ouyang (✉) · Y. Zhou
Institute for Advanced Ceramics, Department of Materials Science, Harbin Institute of Technology, Harbin 150001, China
e-mail: ouyangjh@hit.edu.cn

et al. [9, 10] synthesized $Gd_{2-x}Nd_xZr_2O_7$ ($0 \leq x \leq 2.0$) by a solid state reaction route, and studied their phase structures and order–disorder transitions by room-temperature XRD, high-temperature XRD, and Raman spectroscopic method. However, no data on thermophysical properties for different $(Nd_xGd_{1-x})_2Zr_2O_7$ solid solution systems were reported in open literatures. Therefore, it is of great significance to investigate the thermophysical properties of $(Nd_xGd_{1-x})_2Zr_2O_7$ ceramics system at elevated temperatures.

In the present study, $(Nd_xGd_{1-x})_2Zr_2O_7$ ($x = 0$, 0.1, 0.3, 0.5, 0.7, 0.9, 1.0) ceramic powders were synthesized by the chemical-coprecipitation and calcination method. $(Nd_xGd_{1-x})_2Zr_2O_7$ ceramics were then prepared by pressureless sintering at 1,600 °C. The microstructure and thermophysical properties of different $(Nd_xGd_{1-x})_2Zr_2O_7$ ceramics were examined.

Experimental procedure

Preparation and characterization of $(Nd_xGd_{1-x})_2Zr_2O_7$ powders and bulk ceramics

In the present study, gadolinium oxide powder (Rare-Chem Hi-Tech Co., Ltd., Huizhou, China; purity $\geq$ 99.99%), neodymium oxide powder (Rare-Chem Hi-Tech Co., Ltd., Huizhou, China; purity $\geq$ 99.99%), and zirconium oxychloride (Zibo Huantuo Chemical Co. Ltd., China; Analytical) were chosen as the reactants. Ceramic powders of $(Nd_xGd_{1-x})_2Zr_2O_7$ ($x = 0$, 0.1, 0.3, 0.5, 0.7, 0.9, 1.0) were synthesized by chemical-coprecipitation and calcination method. For each composition, gadolinium oxide and neodymium oxide were weighed and dissolved in diluent nitric acid, while zirconium oxychloride was dissolved in distilled water. Gadolinium oxide and neodymium oxide powders were calcined at 900 °C for 2-h to remove adsorbed water and carbon dioxide before weighing, respectively. These solutions were mixed in appropriate proportions and stirred for 60 min. The precursor solution was slowly added under stirring to excessive diluted ammonium hydrate solution with a pH value of 12.5 to obtain gel-like precipitates. These gels were filtered and washed with distilled water several times to a pH value of 7, and then washed with absolute alcohol for twice. The washed precipitates were dried at 100 °C for 24 h. The remaining solid was then calcined at 800 °C for 5 h for crystallization in air. The powders acquired were first molded under the uniaxial stress. Subsequently, the molded samples were further compacted by the cold isotropic pressing (CIP) method with a pressure of 280 MPa for 5 min. The compacts were then pressureless-sintered at 1,600 °C for 10 h in air to obtain dense bulk ceramics.

Crystal-phase identification of the synthesized powders was determined by X-ray diffractometry (XRD, Rigaku D/Max-rB, Japan) with monochromatized CuKα radiation at a scan rate of 10°/min, and the morphologies of ceramic powders were observed by scanning electron microscopy (SEM, Hitachi S-4700, Japan). The phases of the sintered bulk ceramics were also characterized by X-ray diffraction (XRD,Rigaku D/Max 2200VPC, Japan) with monochromatized CuKα radiation at a scan rate of 4°/min, and the diffraction patterns on single peak of $(622)_{Py}/(311)_F$ were recorded in a step scan mode with a step width of 0.02° and a step time of 3-s. The bulk density of the samples was measured by the Archimedes method with an immersion medium of deionized water. The theoretical density of each solid solution composition was calculated using lattice parameters acquired from XRD results and the molecular weight in a unit cell. Thin foils for transmission electron microscopy (TEM, Philips CM-12, the Netherlands) observations were prepared using the procedure including slicing, polishing, and argon beam milling. A thin carbon coating was evaporated onto the thin foils for electrical conductivity. The microstructures of the sintered specimens were observed by scanning electron microscopy (SEM, FEI Quanta 200, USA). The specimens were polished with 1-μm diamond paste and then thermally etched at 1,500 °C for 1 h in air for SEM observations.

Thermal properties measurements

The linear thermal expansion coefficients of the sintered ceramics were determined with a high-temperature dilatometer (Model Netzsch DIL 402C, Germany) from room temperature to 1,400 °C in an argon atmosphere. Data were continuously recorded at a heating rate of 5 °C/min during heating, and they were corrected using the known thermal expansion coefficient of a certified standard alumina. The specimens have dimensions of about 4 mm × 4 mm × 20 mm.

The thermal diffusivity of the sintered samples was measured using the laser-flash method (Model Netzsch LFA 427, Germany) from room temperature to 1,400 °C in an argon atmosphere. The sample was about 12.7 mm in diameter and about 1.5 mm in thickness. Each sample was ground so that both surfaces were coplanar. Before thermal diffusivity measurement, both the front and the back faces of the specimen were coated with a thin layer of sprayed colloidal graphite. This coating was done to minimize the radiative transport of the thermal flash through the samples and to prevent direct transmission of the laser beam through the translucent specimens at high temperature. Appropriate corrections were made in the thermal diffusivity calculations to account for the presence of these layers. The thermal diffusivity measurement of the specimen was

carried out three times at each temperature level, and the experimental uncertainty is within 5%. The specific heat capacities were determined as a function of temperature from the chemical compositions of $(Nd_xGd_{1-x})_2Zr_2O_7$ ceramics and the heat capacity data of the constituent oxides (Nd_2O_3, Gd_2O_3 and ZrO_2) obtained from the literature [11] in conjunction with the Neumann-Kopp rule [12].

The thermal conductivity k is given by Eq. 1 with the heat capacity Cp, density ρ, and thermal diffusivity λ

$$k = Cp\lambda\rho \quad (1)$$

As the sintered specimen was generally not fully (100%) dense, the measured thermal-conductivity value was modified for the actual data k_0 using the Eq. 2 [13]

$$\frac{k}{k_0} = 1 - \frac{4}{3}\varphi \quad (2)$$

where φ is the fractional porosity.

Results and discussion

Characterization of $(Nd_xGd_{1-x})_2Zr_2O_7$ ceramic powders

The X-ray diffraction patterns of $Gd_2Zr_2O_7$ powders calcined at different temperatures for 2 h are given in Fig. 1. It can be seen that the $Gd_2Zr_2O_7$ powder completely crystallizes at 800 °C. The XRD patterns of different $(Nd_xGd_{1-x})_2Zr_2O_7$ ceramic powders calcined at 800 °C for 5 h are shown in Fig. 2. All the ceramic powders have wide diffraction peaks, and only exhibit a cubic-phase structure, owing to fine grains of $(Nd_xGd_{1-x})_2Zr_2O_7$ powders. Figure 3 shows the typical morphologies of different $(Nd_xGd_{1-x})_2Zr_2O_7$ ($x = 0$, 1.0) powders. From SEM observations, it is seen that $(Nd_xGd_{1-x})_2Zr_2O_7$ ($x = 0$, 1.0) ceramic powders have a particle size of about 100–200 nm in diameter and exhibit to a certain extent some agglomeration.

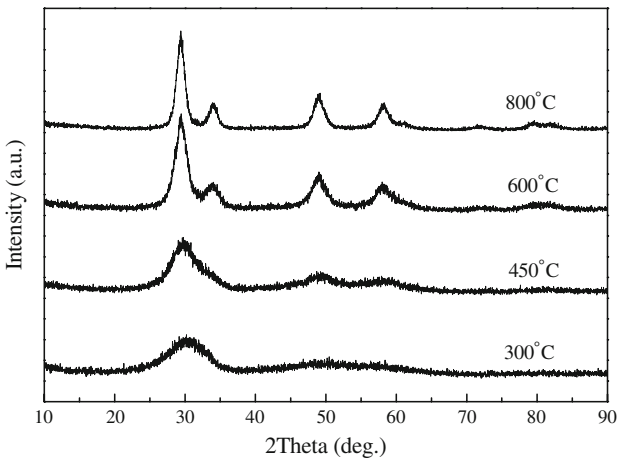

Fig. 1 XRD patterns of $Gd_2Zr_2O_7$ powders calcined at different temperatures for 2 h

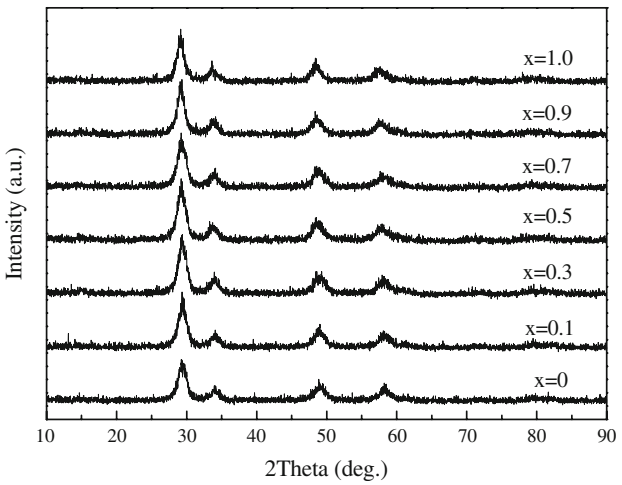

Fig. 2 XRD patterns of different $(Nd_xGd_{1-x})_2Zr_2O_7$ ($x = 0$, 0.1, 0.3, 0.5, 0.7, 0.9, 1.0) ceramic powders calcined at 800 °C for 5 h

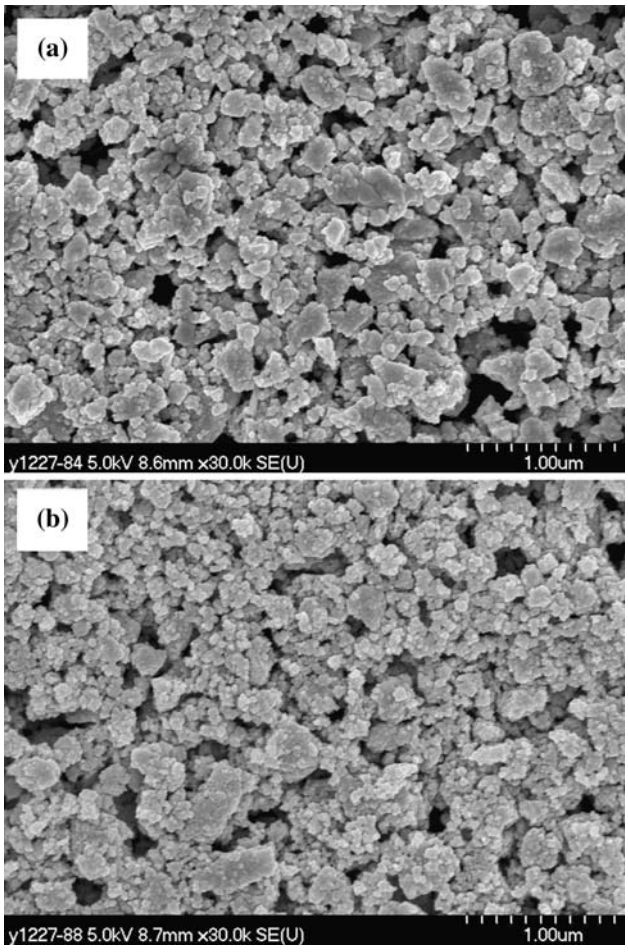

Fig. 3 Morphologies of different $(Nd_xGd_{1-x})_2Zr_2O_7$ ($x = 0$, 1.0) ceramic powders: (**a**) $x = 0$; (**b**) $x = 1.0$

Characterization of different $(Nd_xGd_{1-x})_2Zr_2O_7$ bulk ceramics

To obtain densified samples of $(Nd_xGd_{1-x})_2Zr_2O_7$ ceramics for the determination of thermophysical properties, the ceramic powders were first cold isostatically pressed at 280 MPa, and then pressureless-sintered at 1,600 °C for 10 h. The relative densities of different $(Nd_xGd_{1-x})_2Zr_2O_7$ bulk ceramics are shown in Table 1. The relative densities of the $(Nd_xGd_{1-x})_2Zr_2O_7$ bulk ceramics are over 95% except for $Gd_2Zr_2O_7$, which has a lowest relative density of 92.3%. Figure 4 reveals the X-ray diffraction patterns of different $(Nd_xGd_{1-x})_2Zr_2O_7$ bulk ceramics. It can be seen that all the $(Nd_xGd_{1-x})_2Zr_2O_7$ bulk ceramics are with a single-phase structure. $Gd_2Zr_2O_7$ exhibits a defective fluorite-type structure. With the incorporation of large Nd^{3+} ions instead of small Gd^{3+} ions, $(Nd_xGd_{1-x})_2Zr_2O_7$ ($0.1 \leq x \leq 1.0$) ceramics transform into an ordered pyrochlore-type structure, which is characterized by the presence of typical superlattice peaks at 2θ values of about 14° (111), 28° (311), 37° (331), and 45° (511) using Cu Kα radiation [9], as shown in Fig. 4.

In the $Ln_2Zr_2O_7$ system, the extent of structural order/disorder in these solid solutions is mostly governed by the ion size difference between Ln and Zr sites, that is, by the ionic radius ratio of $r(Ln^{3+})/r(Zr^{4+})$. The pyrochlore structure stability field at an atmospheric pressure in zirconates is limited to the range of $1.46 \leq r(Ln^{3+})/r(Zr^{4+}) \leq 1.78$ [14]. The ionic radius of Zr^{4+} is 0.72 Å in six-coordinated; however, the ionic radii of Gd^{3+} and Nd^{3+} are 1.053 and 1.109 Å in eight-fold coordination, respectively [15]. The average ionic radius, $r(Ln^{3+}_{av.})$, of the Ln-site in the $(Nd_xGd_{1-x})_2Zr_2O_7$ system is estimated from the ionic radius of the component ions and the chemical composition using the following equation [16]:

$$r(Ln^{3+}_{av.}) = xr(Nd^{3+}) + (1-x)r(Gd^{3+}) \quad (3)$$

For $Gd_2Zr_2O_7$, the $r(Gd^{3+})/r(Zr^{4+})$ is equal to 1.46, which resides on the edge of the pyrochlore stability field. It is known that $Gd_2Zr_2O_7$ undergoes a pyrochlore to fluorite (order–disorder) transition when heated above 1,530–1,550 °C. The sintered temperature is 1,600 °C in this investigation, well above this order–disorder transition temperature and the transformation from fluorite to pyrochlore is very slow [17]. Therefore, it is not surprising that the $Gd_2Zr_2O_7$ ceramics exhibit defective fluorite-type structure in this investigation. As for the zirconate solid solutions in the present study, $(Nd_xGd_{1-x})_2Zr_2O_7$, the ratio values of $r(Ln^{3+})/r(Zr^{4+})$ increase as the increase of neodymium content and reach a value of 1.54 for pure $Nd_2Zr_2O_7$ ceramics, which means that, increasing the neodymium content should progressively drive the system toward the ordered pyrochlore-type structure. Therefore, $Gd_2Zr_2O_7$ ceramics have a defective fluorite-type structure, and $(Nd_xGd_{1-x})_2Zr_2O_7$ ($x = 0.1, 0.3, 0.5, 0.7, 0.9, 1.0$) ceramics have an ordered pyrochlore-type structure, as shown in Fig. 4, which is also consistent with the results of Mandal et al. [10].

XRD patterns of different $(Nd_xGd_{1-x})_2Zr_2O_7$ ceramics in a 2θ range of 56° to 59.5° are shown in Fig. 5a, which reveals a single $(622)_{Py}/(311)_F$ peak that shifts gradually to the low angle region for $(Nd_xGd_{1-x})_2Zr_2O_7$ from $x = 0$ ($Gd_2Zr_2O_7$) to $x = 1.0$ ($Nd_2Zr_2O_7$). The lattice parameters calculated from these peaks in relation to the pyrochlore

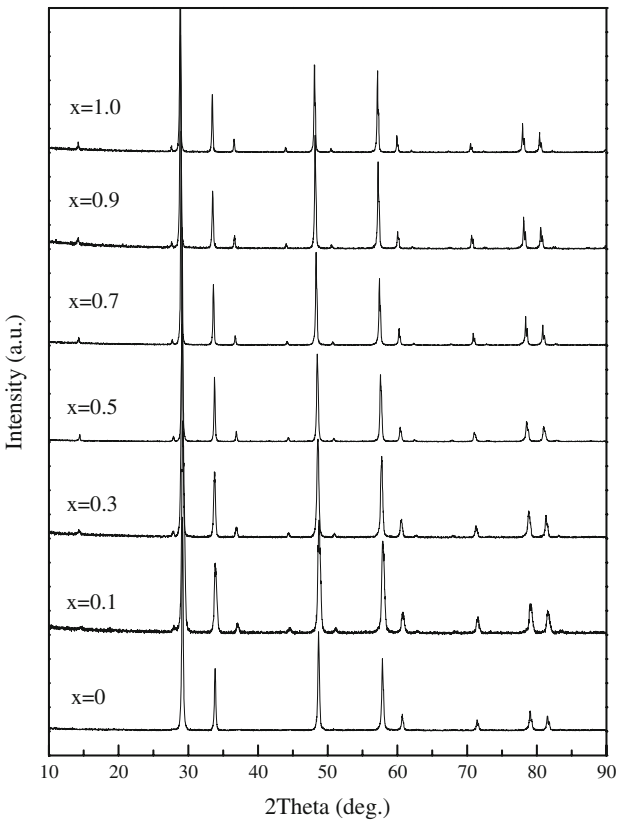

Fig. 4 XRD patterns of different $(Nd_xGd_{1-x})_2Zr_2O_7$ ($x = 0, 0.1, 0.3, 0.5, 0.7, 0.9, 1.0$) bulk ceramics

Table 1 Relative densities of different $(Nd_xGd_{1-x})_2Zr_2O_7$ ($x = 0, 0.1, 0.3, 0.5, 0.7, 0.9, 1.0$) bulk ceramics sintered at 1,600 °C for 10 h

Ceramic bulk materials	Relative densities (%)
$Gd_2Zr_2O_7$	92.3
$(Nd_{0.1}Gd_{0.9})_2Zr_2O_7$	95.3
$(Nd_{0.3}Gd_{0.7})_2Zr_2O_7$	96.9
$(Nd_{0.5}Gd_{0.5})_2Zr_2O_7$	95.1
$(Nd_{0.7}Gd_{0.3})_2Zr_2O_7$	98.2
$(Nd_{0.9}Gd_{0.1})_2Zr_2O_7$	95.6
$Nd_2Zr_2O_7$	97.4

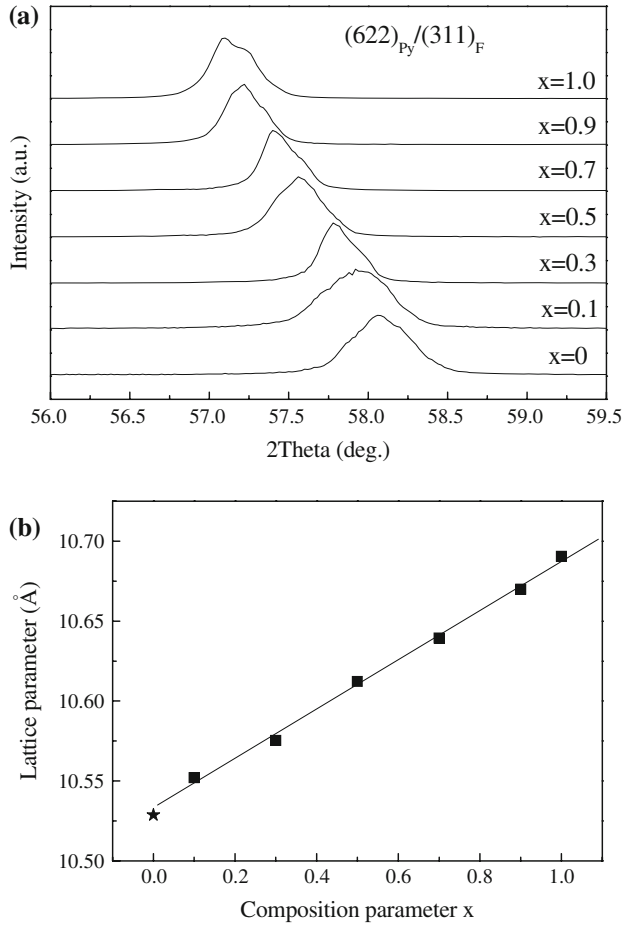

Fig. 5 Fine stepwise XRD patterns and derived lattice parameters of different $(Nd_xGd_{1-x})_2Zr_2O_7$ ceramics: (**a**) a single $(622)_{Py}/(311)_F$ peak in a 2θ range of 56–59.5°; (**b**) lattice parameters derived from (**a**) above. The symbol * in (**b**) marks the composition with a fluorite structure

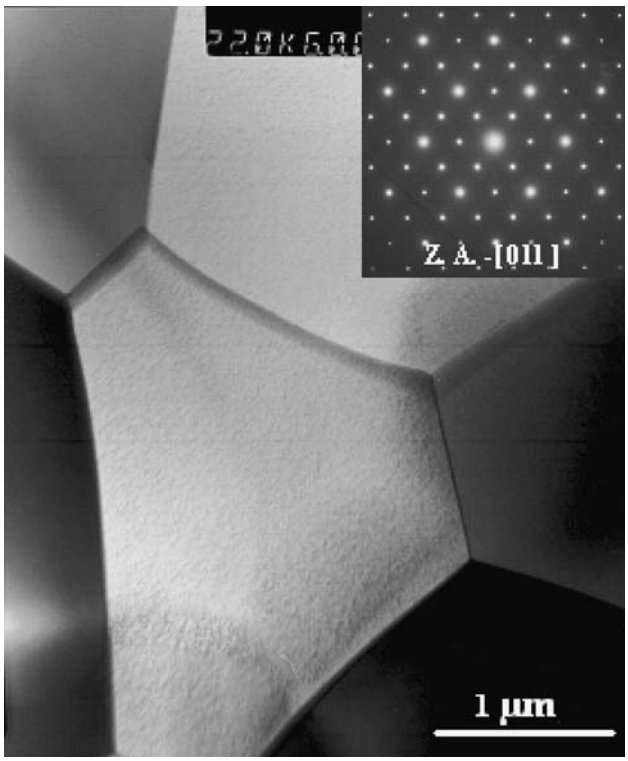

Fig. 6 TEM micrograph and the corresponding [011] zone axis electron diffraction pattern (inset at the upper right) of $NdGdZr_2O_7$ ceramics

unit cell are depicted in Fig. 5b. It can be seen that the approximately linear increase of the lattice parameters with different compositions for $(Nd_xGd_{1-x})_2Zr_2O_7$ system from $x = 0$ ($Gd_2Zr_2O_7$) to $x = 1.0$ ($Nd_2Zr_2O_7$) is in agreement with Vegard's rule [18]. The result indicates that $Gd_2Zr_2O_7$ and $Nd_2Zr_2O_7$ ceramics are infinitely solid solvable. TEM micrograph and the corresponding [011] zone axis selected area electron diffraction (SAED) pattern of $NdGdZr_2O_7$ ceramics are shown in Fig. 6. The SAED pattern indicates that $NdGdZr_2O_7$ ceramics have a superstructure, which is present in the pyrochlore-type structure but absent in a defective fluorite-type structure. Clearly, the grain boundaries of $NdGdZr_2O_7$ ceramics are clean and no other phases are found at the interfaces. Figure 7 shows typical microstructures of different $(Nd_xGd_{1-x})_2Zr_2O_7$ ($x = 0$, 1.0) ceramics. The grains in $(Nd_xGd_{1-x})_2Zr_2O_7$ ceramics are inhomogeneous, and the average grain size is several micrometers. The grain boundaries in different $(Nd_xGd_{1-x})_2Zr_2O_7$ ceramics are very clean and no other phases are found at the interfaces.

Thermal expansion coefficients of $(Nd_xGd_{1-x})_2Zr_2O_7$ bulk ceramics

The thermal expansion coefficient is an important thermal physical property for $(Nd_xGd_{1-x})_2Zr_2O_7$ ceramics. The results of the dilatometric measurement for different $(Nd_xGd_{1-x})_2Zr_2O_7$ bulk ceramics with calibration are shown in Fig. 8. The typical linear expansions are observed for three different $(Nd_xGd_{1-x})_2Zr_2O_7$ ($x = 0$, 0.5, 1.0) bulk ceramics in the temperature range of 25–1,400 °C. Clearly, there is no phase transformation for different $(Nd_xGd_{1-x})_2Zr_2O_7$ bulk ceramics from 25 to 1,400 °C.

The average linear thermal expansion coefficient (α) is defined as the value of the relative length change in the temperature range of $T_1 < T < T_2$, as described by the following equation:

$$\alpha = \frac{(L_2 - L_1)}{L_0(T_2 - T_1)} = \frac{\Delta L}{L_0 \Delta T} \quad (4)$$

where L_0, L_1, and L_2 are the lengths of the specimen at temperatures of T_0 (25 °C), T_1, and T_2, respectively. α is convenient in characterizing the linear expansion of

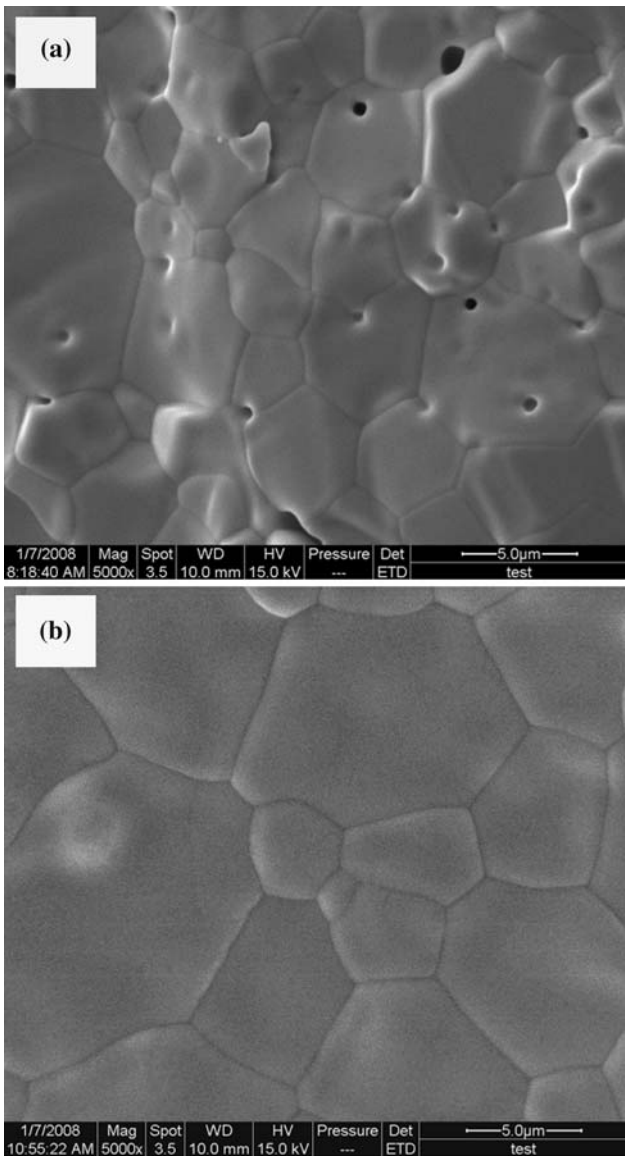

Fig. 7 Microstructures of different $(Nd_xGd_{1-x})_2Zr_2O_7$ ($x = 0$, 1.0) ceramics: (**a**) $x = 0$; (**b**) $x = 1.0$

materials. The average linear thermal expansion coefficients of different $(Nd_xGd_{1-x})_2Zr_2O_7$ bulk ceramics are shown in Table 2 in the temperature range of 25–1,400 °C. The average linear thermal expansion coefficients of different ceramics decrease with the increase of x from $x = 0$ ($Gd_2Zr_2O_7$) to $x = 1.0$ ($Nd_2Zr_2O_7$) for $(Nd_xGd_{1-x})_2Zr_2O_7$ ceramics system in the temperature range of 25–1,400 °C. As reported in the literature [19], the average linear thermal expansion coefficient of $Gd_2Zr_2O_7$ was determined to be 11.60×10^{-6} K^{-1}, which is quite consistent with the corresponding value of 11.56×10^{-6} K^{-1} obtained in our work. The average linear thermal expansion coefficients of different $(Nd_xGd_{1-x})_2Zr_2O_7$ ceramics in this investigation were located within the range of 10.61 to 11.56×10^{-6} K^{-1} from room temperature to 1,400 °C.

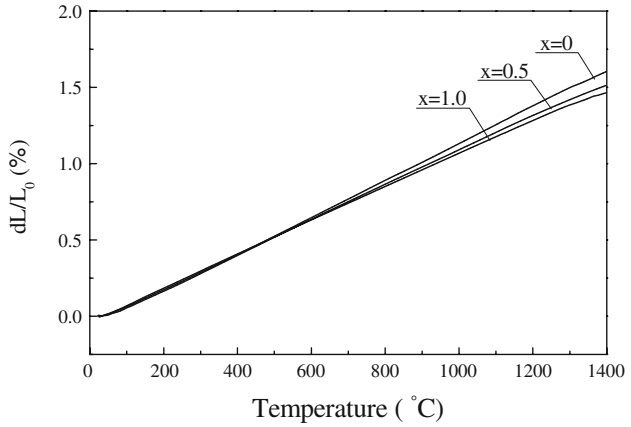

Fig. 8 Calibrated dilatometric data for different $(Nd_xGd_{1-x})_2Zr_2O_7$ ($x = 0$, 0.5, 1.0) bulk ceramics as a function of temperature

Table 2 The average linear thermal expansion coefficients of different $(Nd_xGd_{1-x})_2Zr_2O_7$ bulk ceramics in the temperature range of 25–1,400 °C

Ceramic bulk materials	α (10^{-6} K^{-1})
$Gd_2Zr_2O_7$	11.56
$(Nd_{0.1}Gd_{0.9})_2Zr_2O_7$	10.95
$(Nd_{0.3}Gd_{0.7})_2Zr_2O_7$	10.81
$(Nd_{0.5}Gd_{0.5})_2Zr_2O_7$	10.74
$(Nd_{0.7}Gd_{0.3})_2Zr_2O_7$	10.68
$(Nd_{0.9}Gd_{0.1})_2Zr_2O_7$	10.64
$Nd_2Zr_2O_7$	10.61

Thermal conductivity of $(Nd_xGd_{1-x})_2Zr_2O_7$ bulk ceramics

According to Eq. 1, the values of thermal conductivity are calculated by multiplying specific heat, thermal diffusivity, and density. The high-temperature densities of all specimens were calibrated by the dilatometric measurement data. The variations in thermal diffusivity with temperature for different $(Nd_xGd_{1-x})_2Zr_2O_7$ ceramics are shown in Fig. 9. The values of thermal diffusivity in Fig. 9 are the arithmetic means of three measurements. The error is derived from the mean standard deviation, and the error bars in Fig. 9 are smaller than the symbols. Clearly, the thermal diffusivities of $(Nd_xGd_{1-x})_2Zr_2O_7$ ceramics monotonically decrease with the increase of temperature from room temperature to 800 °C, which suggests a dominant phonon conduction behavior, which is similar to most of the polycrystalline materials [20]. However, above 800 °C, the thermal diffusivities of $(Nd_xGd_{1-x})_2Zr_2O_7$ ceramics showed a slight increase, which was attributed to a small contribution from radiative transport through these specimens at elevated temperatures. In this investigation, the thermal diffusivities of different $(Nd_xGd_{1-x})_2Zr_2O_7$ ceramics were located within

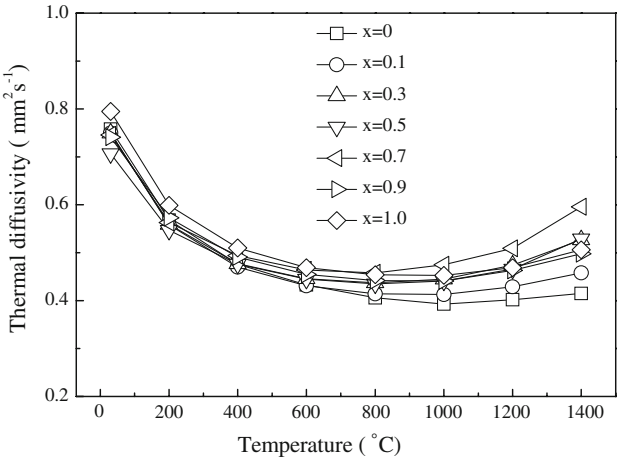

Fig. 9 Thermal diffusivity of different $(Nd_xGd_{1-x})_2Zr_2O_7$ ($x = 0$, 0.1, 0.3, 0.5, 0.7, 0.9, 1.0) bulk ceramics as a function of temperature

the range of 0.39–0.80 mm^2 s^{-1} from room temperature to 1,400 °C.

The calculated thermal conductivities of all specimens are plotted in Fig. 10 according to Eq. 1. The values in Fig. 10 are corrected to 100% theory density according to Eq. 2 and Table 1. The error bars are omitted for the reason that they are smaller than the symbols. The thermal conductivities of different $(Nd_xGd_{1-x})_2Zr_2O_7$ ceramics gradually decrease with the increase in temperature up to 800 °C, which is attributed to the lattice thermal conduction. However, the thermal conductivities increase very slightly above 800 °C for these specimens, which may be attributed to the increased radiation contribution, also known as photon thermal conductivity, with the increase of temperature [21]. The thermal conductivity of $(Nd_{0.7}Gd_{0.3})_2Zr_2O_7$ ceramics increase rapidly than other ceramics above 800 °C, because it has the highest relative density than other ceramics as shown in Table 1. The thermal conductivities of $(Nd_xGd_{1-x})_2Zr_2O_7$ ceramics in this investigation were located within the range of 1.33–2.04 W m^{-1} K^{-1} from room temperature to 1,400 °C, which are clearly lower than those of fully dense 7 wt.%Y_2O_3–ZrO_2 (3.0 at room temperature to 2.3 W m^{-1} K^{-1} at 700 °C reported by Wu et al. [7]). Thus, $(Nd_xGd_{1-x})_2Zr_2O_7$ ceramics are potential candidates for high-temperature thermal-insulation applications.

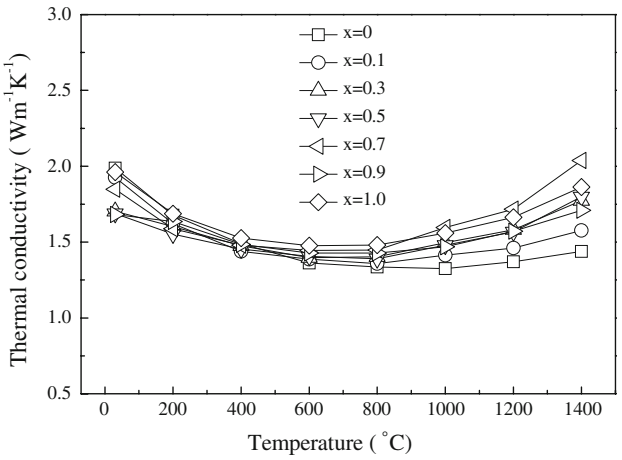

Fig. 10 Thermal conductivity of different $(Nd_xGd_{1-x})_2Zr_2O_7$ ($x = 0$, 0.1, 0.3, 0.5, 0.7, 0.9, 1.0) bulk ceramics as a function of temperature

Conclusions

(1) Ceramic powders of $(Nd_xGd_{1-x})_2Zr_2O_7$ ($x = 0$, 0.1, 0.3, 0.5, 0.7, 0.9, 1.0) with a particle size of about 100–200 nm were synthesized by chemical-coprecipitation and calcination method.

(2) The relative densities of all the sintered samples are in the range of 92.3–98.2%. $(Nd_xGd_{1-x})_2Zr_2O_7$ ($0.1 \leq x \leq 1.0$) ceramics are with a pyrochlore-type structure; however, pure $Gd_2Zr_2O_7$ exhibits a defective fluorite-type structure.

(3) The average linear thermal expansion coefficients of different $(Nd_xGd_{1-x})_2Zr_2O_7$ ceramics decrease with the increase of x value from $x = 0$ ($Gd_2Zr_2O_7$) to $x = 1.0$ ($Nd_2Zr_2O_7$) in the temperature range of 25–1,400 °C. The average linear thermal expansion coefficients of different $(Nd_xGd_{1-x})_2Zr_2O_7$ ceramics were located within the range of 10.61–11.56 $\times$ 10^{-6} K^{-1} from room temperature to 1,400 °C.

(4) The thermal conductivities of $(Nd_xGd_{1-x})_2Zr_2O_7$ ($x = 0$, 0.1, 0.3, 0.5, 0.7, 0.9, 1.0) ceramics first decrease gradually with the increase of temperature and then slightly increase above 800 °C due to the increased radiation contribution with increasing temperature. The thermal conductivities of $(Nd_xGd_{1-x})_2Zr_2O_7$ ceramics were located in the range of 1.33–2.04 W m^{-1} K^{-1} from room temperature to 1,400 °C.

Acknowledgements The authors would like to thank the financial support of the Program of Excellent Teams in Harbin Institute of Technology (HIT) and the Start-up Program for High-level HIT Faculty Returned from Abroad.

References

1. Padture NP, Gell M, Jordan EH (2002) Science 296:280
2. Belmonte M (2006) Adv Eng Mater 8:693
3. Cao XQ, Vassen R, Stoever D (2004) J Eur Ceram Soc 24:1
4. Zhu D, Miller RA (2004) Int J Ceram Technol 1:86
5. Wu J, Wei XZ, Padture NP et al (2002) J Am Ceram Soc 85:3031
6. Suresh G, Seenivasan G, Krishnaiah MV et al (1998) J Alloys Compd 269:L9
7. Vassen R, Cao XQ, Tietz F et al (2000) J Am Ceram Soc 83:2023
8. Lehmann H, Pitzer D, Pracht G et al (2003) J Am Ceram Soc 86:1338
9. Mandal BP, Tyagi AK (2007) J Alloys Compd 437:260

10. Mandal BP, Banerji A, Sathe V et al (2007) J Solid State Chem 180:2643
11. Kubaschewsji O, Alcock CB, Spencer PJ (1993) Materials thermochemistry, sixth edn. Pergamon Press, Oxford, pp 257–323
12. Swalin RA (1972) Thermodynamics of solids, second edn. John Wiley & Sons, New York, pp 53–87
13. Schlichting KW, Padture NP, Klemens PG (2001) J Mater Sci 36:3003
14. Diaz-Guillen JA, Diaz-Guillen MR, Almanza JM et al (2007) J Phys Condens Matter 19:356212
15. Rohrer GS (2004) Structure and bonding in crystalline materials. Cambridge University Press, Cambridge, pp 521–525
16. Yamamura H, Nishino H, Kakinuma K et al (2003) Solid State Ionics 158:359
17. Subramanian MA, Aravamudan G, Subba Rao GV (1983) Prog Solid State Chem 15:55
18. Vegard L (1921) Z Phys 5:17
19. Touloukian YS, Kirby RK, Taylor RE et al (1977) Thermal expansion—non-metallic solids, vol 13. IFI/Plenum, New York
20. Berman R (1976) Thermal conduction in solids. Clarendon Press, Oxford, pp 45–101
21. Mansal NP, Zhu DM (2007) Mater Sci Eng A 459:192